



Real-Time Imaging of Liquid Water in an Operating Proton Exchange Membrane Fuel Cell

M. A. Hickner,^{a,*} N. P. Siegel,^a K. S. Chen,^{b,*} D. N. McBrayer,^a D. S. Hussey,^c
D. L. Jacobson,^c and M. Arif^c

^aEnergy, Infrastructure, and Knowledge Systems Center and, ^bEngineering Sciences Center,
Sandia National Laboratories, Albuquerque, New Mexico 87185, USA

^cNational Institute of Standards and Technology, Gaithersburg, Maryland 20899-8461, USA

Neutron imaging experiments were carried out to measure the water content of an operating proton exchange membrane fuel cell (PEMFC) under varying conditions of current density and temperature. It was found that the water content of the PEMFC is strongly coupled to the current density and temperature of the cell. These measurements indicate that changes in water content lag changes in current density by at least 100 s, both when the current density was increased and decreased. Less liquid water was measured in the cells when operating at 80°C than at 40°C. At 60°C cell temperature, a peak in water content was observed around 650 mA/cm² and the water content was found to decrease with increasing current density. This is explained in the context of cell heating by performing a simple thermal analysis of an operating PEMFC so as to yield quantitative information on the waste heat and its effects on the liquid water contained in the cell.

© 2006 The Electrochemical Society. [DOI: 10.1149/1.2184893] All rights reserved.

Manuscript submitted November 28, 2005; revised manuscript received January 11, 2006.
Available electronically March 27, 2006.

Understanding liquid water content and its distribution within an operating proton exchange membrane fuel cell (PEMFC) is critical to designing high-performance systems and formulating rational models for simulating PEMFC behavior. The generation, transport, and removal of liquid water are key phenomena that occur in a PEMFC. Effective water transport through and removal from the membrane electrode assembly (MEA) is crucial to achieving high current density and maintaining PEMFC performance. In the design and optimization of PEMFCs, it is important to be able to quantify the water content in an operating cell in order to gain insight into the dominant phenomena or processes that influence liquid water transport and removal. This work is concerned with the measurement of liquid water in an operating PEMFC under various temperatures, relative humidities, and current densities. Neutron imaging, or radiography, is a useful tool for gaining qualitative and quantitative insight into liquid water content and distribution in near real-time (temporal resolution ~ 1 s).

Both Tuber et al.¹ and Yang et al.² used optical methods for imaging water in PEMFCs under a range of operating conditions. In order to use optical techniques, a transparent fuel cell must be fabricated. Optical imaging is capable of high spatial and temporal resolutions for the elucidation of dynamic processes, but optical techniques suffer from fogging of the transparent window under humidified conditions and it is more difficult (though possible) to obtain quantitative information. Furthermore, optical investigations are limited to studying liquid water in the gas flow channels because that is the only visible water in the fuel cell; liquid water inside the gas diffusion layers (GDLs) cannot be imaged using optical techniques. Tuber et al.¹ were able to correlate the appearance of water in the cell with a drop in current density, although they did not quantify the liquid water in the cell. Yang et al.² focused on the appearance and dynamics of liquid water droplet formation and breakup in the gas flow channels. Their work concentrated on studying microscale phenomena in the channel (the droplets), but whole-cell images were not presented.

Proton nuclear magnetic resonance spectroscopy was utilized by Feindel et al.³ to image the liquid water distribution in an operating PEMFC. This technique is promising because it can distinguish liquid water in the different planes of the MEA. The authors obtained both “face-on” and “side-on” views of the fuel cell. However, this technique is still in its infancy and the experimental procedures must be refined before useful information can be obtained.

Neutron is a powerful technique for imaging liquid water in an operating PEMFC because of the following: (i) conventional cell hardware materials like graphite and aluminum have relatively small neutron-scattering cross sections and so can be used in cell hardware construction; (ii) the spatial resolution of the images is sufficient (approximately 150 μm) to distinguish the main features of a typical PEMFC; (iii) large areas (of order 20 \times 20 cm) can be imaged; (iv) with current detector technology, the temporal resolution can be up to 30 Hz; and (v) images can be gathered and stored over a significant time frame to resolve slow processes in the cell. Two major limitations of employing the neutron imaging technique to detect liquid water in an operating PEMFC are: (i) a neutron source with high fluence rate is required; this is only possible at a few major research facilities across the world, and (ii) present tomographic imaging methods require cell rotation to yield three-dimensional (3D) information on the cell.

Neutron imaging of fuel cells is a relatively new technique, but is poised to become a valuable experimental tool in fuel cell research. Bellows et al.⁴ used neutron imaging to measure the water content profile in a Nafion membrane. In these experiments, the cell was imaged “side-on” to allow water content measurement of the membrane. In most other neutron imaging studies, as in this report, the cell is imaged “face-on” to measure the water content across the active area of the MEA. Perhaps the first report of using neutron imaging for investigation of liquid water and two-phase flow in an operating PEMFC was by Geiger et al.⁵ These authors explored the performance of both hydrogen/air and direct methanol fuel cells (DMFCs). They were able to image the water content of hydrogen/air cells during startup and shutdown and were also able to locate exactly where liquid water was present during these processes. Under the conditions of their study, they reported that liquid water was mainly observed in the anodic flow channels of the hydrogen-fueled cell. The gas retention in the DMFC flow fields was found to vary greatly with flow direction. No quantitative data for water content were presented by Geiger et al.⁵ Kramer et al.⁶ extended the investigations of DMFCs further and were able to detect nonuniformities in the distribution of reactants across the fifty parallel flow channels in the anode compartment. They also observed the high tendency of the cathode compartment to flood with liquid water and demonstrated the quantitative analysis of water content in an operating PEMFC.

Kramer et al.⁷ demonstrated the potential for neutron imaging to reveal the relationship between water content in a PEMFC and operating current density. They were able to quantify the water content and plot current density vs liquid water volume. Additionally, they presented water content profiles as the liquid water evolving in an

* Electrochemical Society Active Member.

^z E-mail: mahickn@sandia.gov

operating cell. Based on their measurements, Kramer et al.⁷ found increasing liquid water content toward the outlet of the cell for a cell temperature of 70°C and gas feeds with dew points of 55 and 65°C, respectively. This result could be expected for gas feeds of less than 100% relative humidity.

Pekula et al.⁸ reported neutron radiographs of operating fuel cells and observed liquid water concentrating near the exit of the cells. The water content is seen to qualitatively increase with decreasing cathode flow stoichiometry. This might indicate that the majority of the liquid water measured under these conditions was in the cathode compartment rather than in the anode compartment, as observed by Geiger et al.⁵ Chuang et al.⁹ examined the correlation between flooding behavior as measured by polarization curves and neutron images. They reported that the loss of 115 mV in cell performance was due to an increase in water content of 175 mg of water over a 50-cm² active area. Additionally, Chuang et al.⁹ distinguished liquid water present in the flow channels from that present under the lands of the flow fields by masking the images during data analysis. They found in most cases that more liquid water was concentrated under the lands than in the channels.

Satija et al.¹⁰ used masking techniques to show that the water in their PEMFC system resided mainly on the cathode side of the cell. These authors also showed the water content in a PEMFC as a function of time over 2000 s. It was determined that both the water in the flow channels and the water under the channel lands show the same trend with time, indicating that the water in these two regions may undergo some of the same filling and removal processes.

In the present work, neutron imaging was used to quantify the liquid water content and its distribution in an operating PEMFC under a range of conditions. The present work differs from prior research efforts as reported in the literature in that it focuses on two important aspects: (i) transient behavior of liquid water transport within a PEMFC; and (ii) effects of local heating on liquid water content and distribution under a variety of conditions. The objective of the present work is to elucidate the effects of temperature and current density and their interplay with local heating and liquid water content of a PEMFC.

Experimental

The imaging instrument and setup used in this experiment is similar to that of Satija et al.¹⁰ However, instead of a neutron imaging charge-coupled device (CCD) camera, a flat panel amorphous silicon detector with 127- μm pixel pitch and a 3-Hz image acquisition rate was utilized for these experiments.

The raw image data was analyzed using the IDL programming language (RSI, Inc., Boulder, CO^d) with specialized analysis routines developed at the National Institute of Standards and Technology, NIST, (contact daniel.hussey@nist.gov). Two approaches were explored for presentation and interpretation of the neutron imaging data. The first approach dealt with taking two separate sets of data: “dry” images, and “wet” images. The dry images were taken after the MEA had been dried in the cell hardware for at least 8 h with dry flowing gas at the cell temperature of interest (same temperature as the wet images to account for thermal expansion of the hardware). The wet images were taken during normal fuel cell operation under conditions of constant current after equilibration for at least 30 min. Applying Beer’s law, the total water thickness is obtained from the natural log of the ratio of the wet to dry intensities. In these images, all the cell features that do not change with water content (cell hardware, background features) are subtracted and not visible in the resulting image. This type of data analysis is referred to as a “dry reference” in the present work.

^dCertain trade names and company products are mentioned in the text or identified in an illustration in order to adequately specify the experimental procedure and equipment used. In no case does such identification imply recommendation or endorsement by NIST, nor does it imply that the products are necessarily the best available for this purpose.

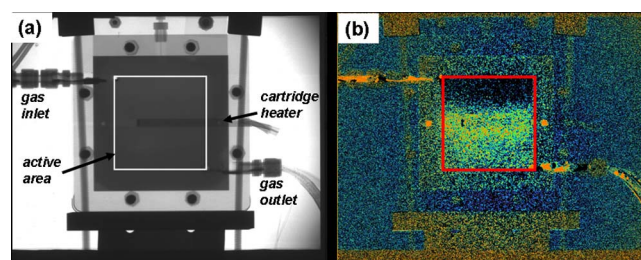


Figure 1. (Color) Neutron images of a 50-cm² fuel cell showing (a) the cell construction, gas ports, and active area outlined in white, and (b) a colorized image showing the active area outlined in red. Red, orange, and green colors correspond to maximum water, blue, and black correspond to minimum water.

The other method for analyzing the neutron imaging data was to measure an “internal reference” at open-circuit voltage (OCV) under the conditions of interest. In general, the cell was left to equilibrate for 30 min at open circuit under the conditions of interest (temperature, humidity, gas flow rates). Image acquisition commenced with the cell remaining at open circuit followed by a change in cell current after 30 s (for steps) or 2 min (for polarization curves). In step experiments, the cell current was then held constant for the remainder of the test (typically 10 min) and for polarization curves, the current was increased at 2-min intervals. The open-circuit liquid water content was then subtracted from the data set to allow for the visualization and calculation of the change in water content in the cell due to the increase in current density relative to open-circuit conditions (zero load). This is termed the change in water volume (or content) and is referred to as $\Delta V_{\text{H}_2\text{O}}$. The reference condition, dry cell or open circuit, is noted for all of the results presented.

All experiments were conducted utilizing 50-cm² cell hardware and a fuel cell test station (both from Fuel Cell Technologies, Albuquerque, NM). The flow fields used were single-channel serpentine in a coflow anode and cathode pattern. All cells were fed with gases at constant flow rates of 1140 std cm³/min H₂ for the anode and 2700 std cm³/min air for the cathode. The outlet pressure of both anode and cathode was maintained at 1.4 bar gauge (20 psig). The MEAs were made in-house at Sandia National Laboratories utilizing Nafion 112 membranes and standard thin-film electrodes¹¹ with Pt catalyst loadings of 0.17 mg/cm² on the anode and cathode. The catalyst utilized was 20% Pt on XC-72 (E-TEK, Sommerset, NJ) and 300 μm thick carbon paper with integral microporous layers were used as GDLs.

Grayscale and colorized images of the cell are shown in Fig. 1, which details the location of each of the cell components. Figure 1a shows a grayscale intensity image (light regions are less attenuation, dark regions are more attenuation) of the dry fuel cell hardware. Both the gas inlet and outlet tubes are visible as well as the cartridge heater, thermocouple, and other cell hardware. Multiple fans were placed outside of the image to cool the cell to the desired set point temperature when necessary. Figure 1b is a colorized density image of an operating fuel cell containing water in the active area. Red color corresponds to maximum water content; black corresponds to minimum water content. Liquid water is visible in the inlet and outlet tubes because they are slightly cooler than the cell. The cell hardware and other features that do not change with water content are only slightly visible in Fig. 1b because of the OCV reference used to create this image. Both full-cell view and cropped images showing just the active area are presented.

Results and Discussion

Transient behavior.— Figure 2 shows a series of images obtained during a step change in cell current density from 0 mA/cm² (open circuit) to 1500 mA/cm². All of the images in Fig. 2 are referenced to the open-circuit conditions recorded at the beginning

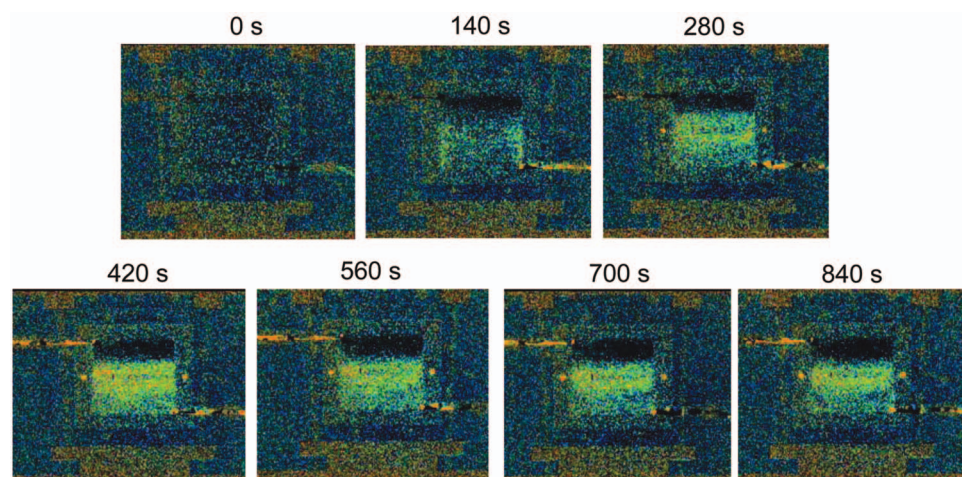


Figure 2. (Color) Images of increasing water content in a PEMFC during a current step from 0 to 1500 mA/cm² occurring at time 30 s. Cell temperature 80°C; 100% RH gas feeds; 1.4 bar gauge outlet pressure; 1140 std cm³/min H₂; 2700 std cm³/min air.

of the experiment therefore, the extra liquid water that results from operation of the cell is shown in this series of images. The step change in cell current was triggered 30 s into the data collection of the images. The current and voltage of the cell were recorded during the course of the experiment and are shown in Fig. 3.

The first image in Fig. 2 at 0 mA/cm² is nearly dark in the active area, which is expected because the open-circuit condition is used as the reference image. At 140 s, when the cell has been operated at 1500 mA/cm² for 110 s, liquid water is seen to appear at the bends in the channels. As the cell continues to operate, liquid water accumulates and reaches an approximately steady profile at about 150–200 s. A plot of the water content in the cell as a function of time is shown in Fig. 4. Comparing the changes in voltage and current shown in Fig. 3, and the increase in water content, it is apparent that the water content of the cell responds much more slowly to changes in current density than the electrical response of the cell. Under conditions where the cell reactant feeds are highly humidified, slugs of liquid water may pass through the cell; Figs. 2 and 4 show evidence of this process occurring at about 420 s. When this happens, the overall water content is seen to rapidly increase and then return to an equilibrium value within 100 s or less.

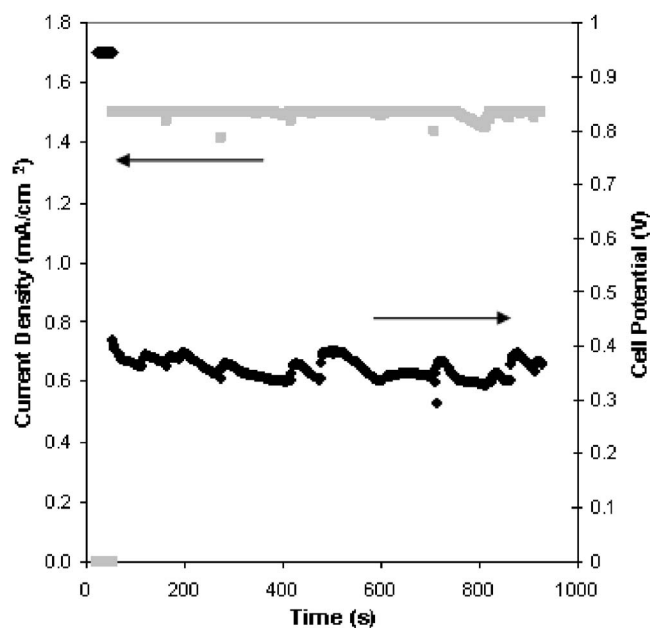


Figure 3. Voltage and current response of cell at 80°C. Current instantaneously stepped from 0 to 1500 mA/cm² at time 30 s.

The filling and draining of a cell with water in response to a step change in current density was measured at a cell temperature of 40°C. Figure 5 shows the additional water volume accumulated in the cell due to a step change in current density from OCV to 1000 mA/cm² at 300 s, as well as the drainage curve when the current is stepped down from 1000 mA/cm² to OCV 600 s. As demonstrated previously at 80°C, the cell is slow to fill with water when the current is increased instantaneously and requires around 200 s in order for the water content to begin to reach a steady-state value. In order to reach steady state, the rate of liquid water production in the cell must be exactly balanced by the rate of liquid water removal. The removal rate is influenced by the capillary transport rate of liquid water through the GDL insofar as liquid water produced in the catalyst layers must first move through the GDL to the gas flow channel (GFC) where it may be removed from the cell by evaporation or advection. The link between the liquid water response of the cell following a step change in current and the transport of liquid water through the GDL can be further illustrated by considering a time constant for capillary water transport in the GDL. This lag in water content of the cell behind the current density change is reasonable if the time constant of capillary water diffusion in the GDL is considered. Mazunder and Cole¹² used a maximum value of 10⁻⁴ cm²/s for the capillary diffusion coefficient, D_c . As expected,

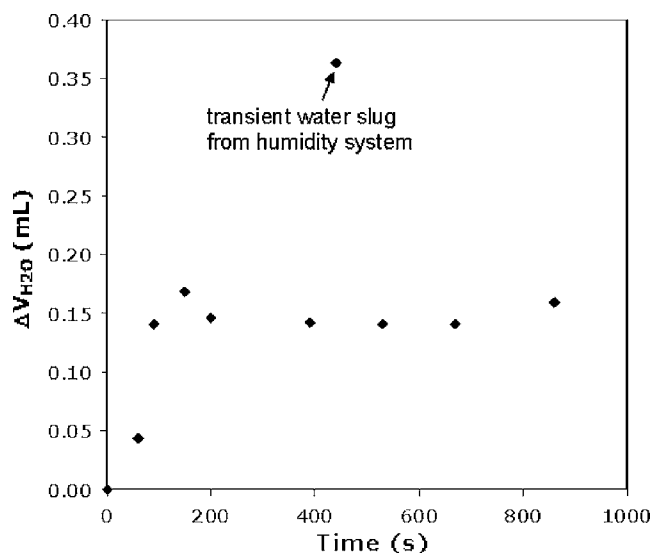


Figure 4. Change in total water content of the cell when the current was stepped from 0 mA/cm² to 1500 mA/cm² at time 30 s.

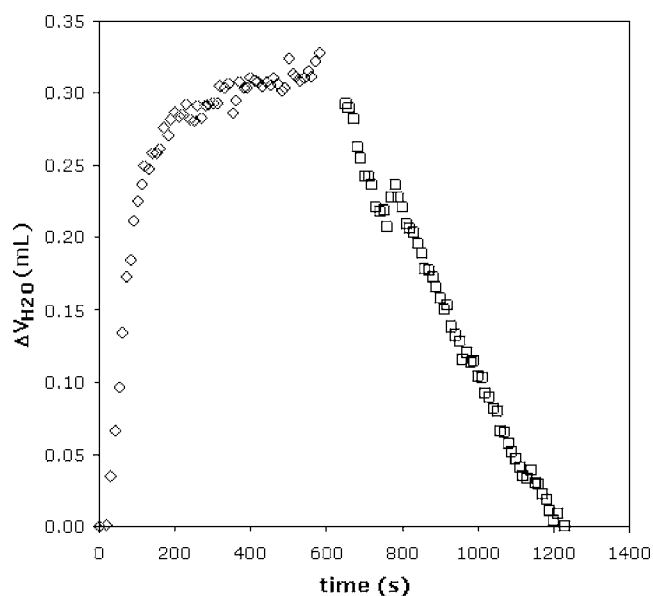


Figure 5. Change in water content during a step up in current density from 0 to 1000 mA/cm² occurring at 300 s (\diamond) and a step down in current density from 1000 to 0 mA/cm² occurring at 600 s (\square). Cell temperature 40°C.

the value for D_c is a function of saturation level. With $D_{c,max} = 10^{-4}$ cm²/s, D_c ranges from 10^{-4} to 10^{-5} cm²/s, as shown in Fig. 2 of Ref. 12 for saturation between 2 and 85%.¹² Because the filling and draining experiment was performed with saturated feed streams, a value of 10^{-5} cm²/s may be a good value for the purpose of estimating a liquid water diffusion characteristic time under the experimental conditions. Now, with $D_c = 10^{-5}$ cm²/s and $L = 300$ μ m (thickness of GDL) = 0.03 cm, we can estimate the characteristic time for capillarity-driven liquid water diffusion to be

$$\frac{L^2}{D} = \frac{(0.030 \text{ cm})^2}{10^{-5} \text{ cm}^2 \text{ s}^{-1}} = 90 \text{ s} \quad [1]$$

In the first 90 s of the filling and draining experiment shown in Fig. 5, there is a large increase in the water content of the cell. This may correspond to the GDL filling up with liquid water. The small increase after the first 90 s may be droplets forming in the gas flow

channels. When the current is ceased, the cell empties water very slowly and does not reach steady state in the course of the 600-s experiment. Because the gas feeds to the cell were at 100% relative humidity (RH), the only method for water removal is the advection of liquid water from the flow channels. This experiment illustrates that once liquid water is in the GDL, it is difficult to remove by advection.

The distribution of liquid water throughout the active area of the cell is an important phenomenon that has not received much attention in the literature and not much data have been reported. The liquid water distribution across the active area can be quantified using the neutron images. Shown in Fig. 6 are two images of the cell taken at two different times (70 and 830 s) during a step experiment from 0 mA/cm² to 1500 mA/cm² at 80°C and a corresponding plot of the water content profile from inlet to outlet. The distribution of liquid water throughout the cell is determined by the interplay between the local current density (and associated water generation), local heating (heat produced by the cell), and reactant depletion down the flow channel. The term local heating is used to describe the increase in MEA temperature due to waste heat generated by the cell via reversible heating and cell overvoltages. This phenomenon is discussed in more detail in the second portion of this paper. In the context of Fig. 6, local heating may influence the distribution of liquid water in the cell as follows: Near the inlet, local heating enhances the evaporative removal of liquid water by raising the inlet gas temperature above the value at which it was humidified, effectively dropping its RH. At some point downstream of the inlet, the gas flow becomes saturated and all water produced by the cell remains in liquid form. This is shown in Fig. 6 as an increase in liquid water content near the center of the cell. In segmented cell studies,¹³ the center portion of the cell also shows the maximum current density, which would further increase the amount of liquid water in this region relative to the rest of the cell. The bottom third of the cell experiences reactant depletion and thus lower local current density. This decreases the rate of water production and thus renders the cell relatively dry near the exit. The water distribution trend seen in the 70- and 830-s data is different with regard to both shape and magnitude. This is most likely linked to the response time associated with liquid water accumulation in the cell, previously shown to be on the order of 200 s for a step change in current at 80°C.

Local heating effects.—A frequently observed trend in fuel cell operation is that cell performance increases with cell operating temperature. This change in performance can be attributed to

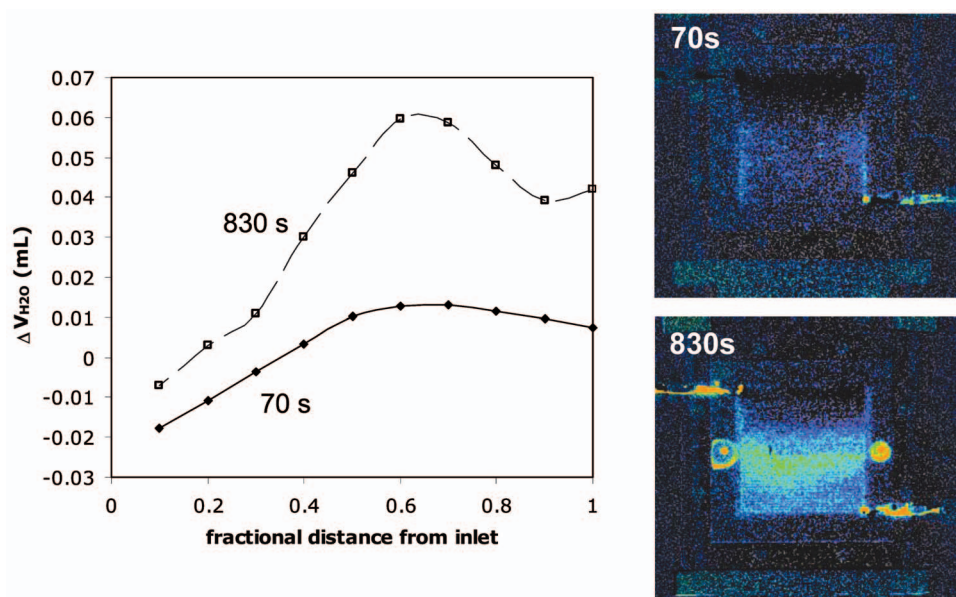


Figure 6. (Color) Change in water content distribution from OCV at 70 and 830 s after a step in current density from 0 to 1500 mA/cm² at time 30 s. 80°C cell temperature. Plot shows the quantitative water content distributions as a function of position in the cell. Images are shown for 70 and 830 s.

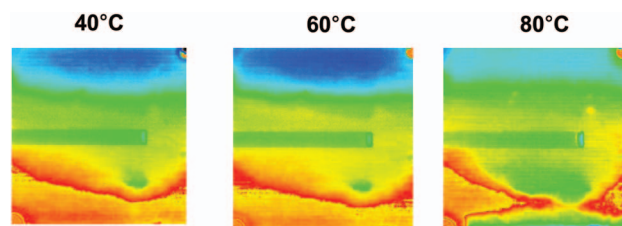


Figure 7. (Color) Active area images showing entire water content (dry reference) for bulk cell temperatures of 40, 60, and 80°C. Red regions in the upper right and lower left corners are the plastic (high neutron cross section) gas inlet and outlet tubes.

temperature-dependent processes occurring within the cell, e.g., reaction kinetics, proton conductivity, gas species diffusion, and phase change. It is reasonable to assume that liquid water transport is also thermally coupled. In this section we present neutron imaging results obtained for cells operating at different temperatures that illustrate the influence of local heating effects on liquid water transport.

Figure 7 shows a steady-state comparison of neutron images taken at three different cell temperatures (40, 60, and 80°C) with equivalent gas flow rates at 100% inlet gas RH (dew point set at the cell temperature) and equivalent average current densities of 1250 mA/cm², with cell voltages of 0.3, 0.41, and 0.45 V, respectively. From these images, which show the entire water content of the cell (dry cell reference), it is evident that more water resides in the cell at lower temperatures than at higher temperatures. The decreased water content in cells operating at higher temperatures is one possible explanation for the frequently observed increase in cell limiting current with temperature.

A further illustration of local heating effects on liquid water transport is observed in a comparison of cell water content at 40 and 80°C following a step change in current density as shown in Fig. 8, in which water content as a function of time is plotted for a step change in current density from 0 to 1000 mA/cm² and from 0 to 1250 mA/cm² for 40 and 80°C, respectively. The cell voltage in both cases under load is 0.52 V. Despite the fact that more water is being produced at 80°C (1250 vs 1000 mA/cm²), there is almost three times as much water present in the cell at 40°C. This suggests that water can be removed from the cell more effectively at higher temperatures.

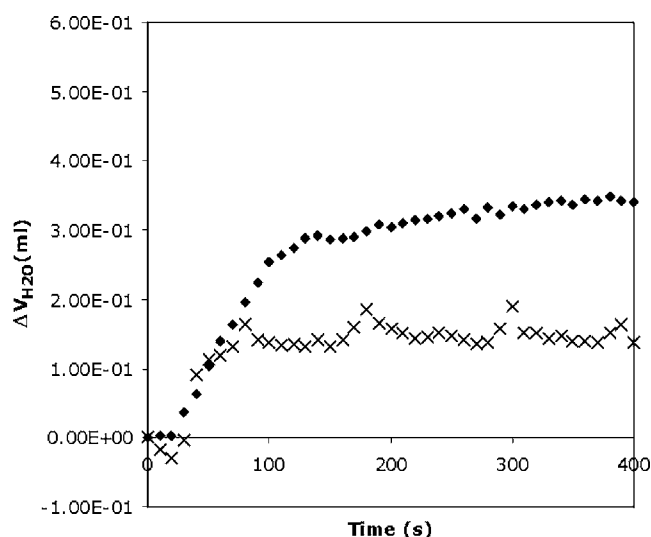


Figure 8. Water content of a PEMFC at 40°C bulk temperature during a step from 0 to 1000 mA/cm² (◇) and 80°C bulk temperature during a step from 0 to 1250 mA/cm² (×).

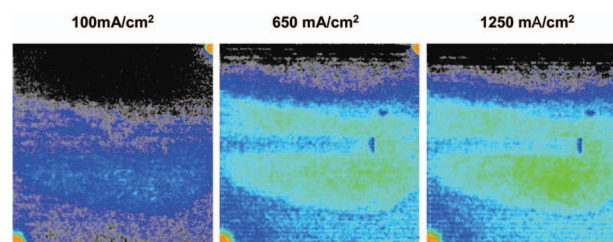


Figure 9. (Color) Active area images of change in water content (open-circuit reference) for a 40°C cell bulk temperature.

Figure 9 shows three images of the active area of a cell operating at 40°C (dew points of inlet gases set to cell temperature) with current densities of 100, 650, and 1250 mA/cm². The images show that water content steadily increases with current density across the entire load range. Figure 10 shows the same experiment repeated for a 60°C cell temperature. In this instance, the maximum water content is observed at 650 mA/cm². A further increase in current density to 1250 mA/cm² leads to a decrease in cell water content. One might assume that because more water is produced as current increases, the total volume of water within the cell should also increase with current. The data indicate that this holds true at 40°C, but not at 60°C, which suggests that there is a temperature-dependent process occurring within the cell that allows for an increase in the rate of liquid water removal from the cell as temperature is increased. One such process involves the evaporation of liquid water within the cell as a result of local heating and the associated temperature rise of the gas flow. We present a simple thermal analysis to illustrate this process.

Under certain conditions, an increase in fuel cell temperature can significantly impact the transport of liquid water within the cell. This effect is most pronounced in the influence of temperature on the ability of flowing gas, such as the cathode inlet flow, to carry water vapor. A measure of this ability is the specific humidity, or the mass ratio of water to air in a gas stream, which is defined in Eq. 2 and plotted in Fig. 11 as a function of temperature

$$\omega = \frac{M_{\text{H}_2\text{O}}}{M_{\text{air}}} \frac{P_v}{P_{\text{tot}} - P_v} \quad [2]$$

If the gas flow at pressure P_{tot} is fully saturated with water vapor, the vapor pressure of water, P_v , is equal to the saturation pressure, which increases nonlinearly with temperature. This gives the humidity ratio a strong, nonlinear dependence on temperature that is evident in Fig. 11. The implication for water transport is that as cell temperature increases, so does the ability of the gas flow to carry water vapor. In addition, for a given change in temperature, the corresponding change in the humidity ratio (the derivative, $d\omega/dT$) increases as the overall temperature increases. For example, if we assume that local heating results in a 4°C temperature rise for a saturated cathode gas flow entering at 40°C, the gas will be able to uptake (by evaporation) an additional 5.13×10^{-3} g of liquid water for each gram of air flow when the gas pressure is 1.4 bar gauge.

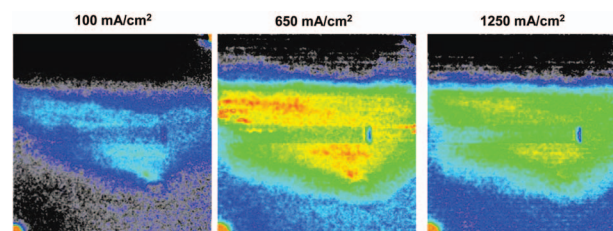


Figure 10. (Color) Active area images of change in water content (open-circuit reference) for a 60°C cell bulk temperature.

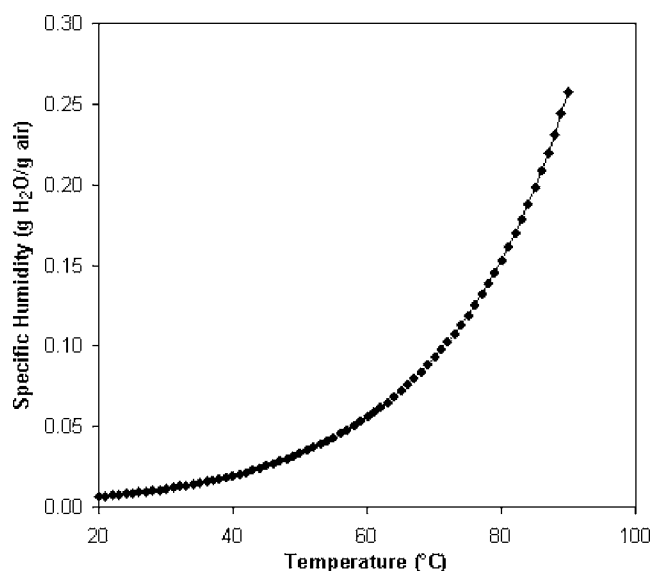


Figure 11. Humidity ratio showing the molar ratio of water to air in a fully humidified gas stream.

If the same 4°C temperature rise is applied to a saturated gas flow entering at 80°C, this flow will be able to uptake an additional 65.9×10^{-3} g of liquid water for each gram of air flow, which is nearly 13 times greater than the 40°C case. The mass flow rate of water vapor in a humidified air stream can be calculated with Eq. 3. The rate of additional water removal due to a change in the specific humidity can be calculated with Eq. 4

$$\dot{m}_{\text{H}_2\text{O}} = \dot{m}_{\text{air}}\omega \quad [3]$$

$$\Delta\dot{m}_{\text{H}_2\text{O}}|_{1-2} = \dot{m}_{\text{air}}(\omega_2 - \omega_1) \quad [4]$$

where subscript 1 corresponds to the inlet temperature and subscript 2 includes the temperature rise of the gas flow associated with local heating. Thermal energy is required to drive the additional evaporation of liquid water at a given temperature. The requisite heat input can be approximated with Eq. 5. This heat is produced by the cell itself, through thermodynamic constraints and cell overvoltages, and can be expressed as shown in Eq. 6-8

$$Q_{\text{evap}} = h_{\text{evap}}\dot{m}_{\text{H}_2\text{O}} \quad [5]$$

$$V_{\text{HHV}} = \frac{\Delta H_{\text{HHV}}^{\text{H}_2}}{2F} \quad [6]$$

$$V_{\text{cell}} = \frac{\Delta G_{\text{HHV}}^{\text{H}_2}}{2F} - \sum_i \eta_i \quad [7]$$

$$Q_{\text{cell}} = (V_{\text{HHV}} - V_{\text{cell}})J \quad [8]$$

V_{HHV} represents the energy content of hydrogen based on its higher heating value and has a value of 1.48 V at 80°C.¹⁴ V_{cell} is the difference between the OCV, expressed as a function of the Gibbs free energy, and the summation of the cell overvoltages. The cell current density is expressed as J . Provided that sufficient thermal energy is present, additional evaporation of liquid water will take place, which opposes electrochemical water production and reduces the net rate at which liquid water is produced at the cathode, as expressed by Eq. 9

$$\dot{m}_{\text{H}_2\text{O}}^{\text{net}} = \frac{JM_{\text{H}_2\text{O}}}{2F} - \dot{m}_{\text{air}}(\omega_2 - \omega_1) \quad [9]$$

The first term in this equation represents the production rate of water via the oxygen reduction reaction. The second term represents addi-

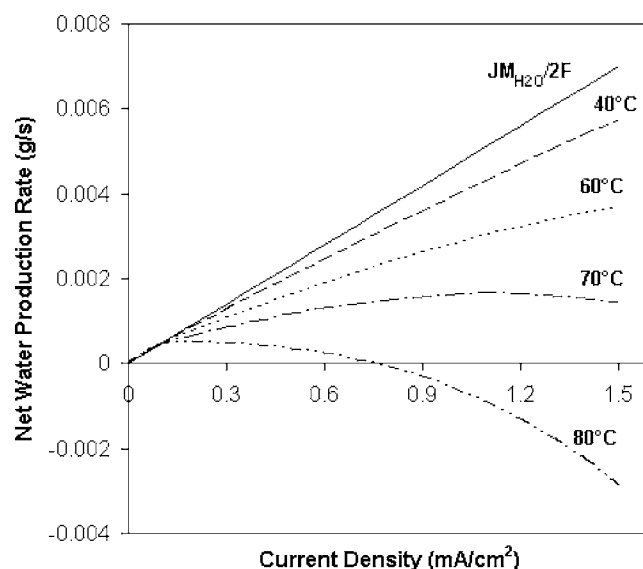


Figure 12. Net water production as a function of current density considering electrochemical water production only ($JM_{\text{H}_2\text{O}}/2F$) and local heating effects at 40, 60, 70, and 80°C.

tional evaporation of liquid water due to local heating. Electro-osmotic transport and back-diffusion of water are neglected in this simple analysis. Although these are both important effects, omission here does not alter the trends that we hope to illustrate.

Figure 12 shows the net water production at the cathode for fuel cells operating at 40, 60, 70, and 80°C. This figure was generated using Eq. 5 with the assumption that the temperature of the cell varies linearly with current production, and the overall increase in temperature was set at 15°C for each case (at maximum current density). In addition, a check on the cell heat output was performed to ensure that sufficient thermal energy was available to drive additional evaporation. The seemingly large rise in local temperature assumed for this analysis has been measured in the electrolyte by Mench et al.¹⁵ at various locations in a 50-cm² fuel cell (from Fuel Cell Technologies) at 0.45 V and 1400 mA/cm², an experimental apparatus and conditions similar to those of this study. Other investigators have predicted similar increases in temperature using a thermal model with experimentally determined thermal conductivities and interfacial resistances.¹⁶ Additionally, during experiments performed in the present study, bulk cell temperature increases of between 4 and 7°C were measured near the outer surface of the cell when the current density was maintained above 1000 mA/cm² for long periods of time (approximately 40 min to 1 h). The internal temperature of the cell was likely significantly higher.

The results in Fig. 12 illustrate two important effects. The first is that for a given amount of current production, fuel cells operating at higher temperatures will have a lower net rate of water production, which likely leads to a corresponding decrease in water content. The second effect is related to the change in water production rate with current density. At 40°C, the net water production rate increases steadily with current density, indicating that the amount of additional evaporation of liquid water is small. The 40°C $JM_{\text{H}_2\text{O}}/2F$ limit is also shown in Fig. 12, which is the rate of liquid water production due solely to oxygen reduction and does not take into account any local heating or evaporative effects. At 60°C, the net rate of water production increases with current but at a slower rate than the 40°C case. At 70°C, a maximum in the water production rate is observed. At 80°C, water production is completely offset by additional water removal due to local heating over most of the current range. This may seem counterintuitive until one considers that water production via oxygen reduction is linear with respect to cur-

rent, whereas the evaporative removal of water is coupled nonlinearly to temperature due to the nonlinear increase in the vapor pressure of water with temperature.

It is possible to explain some of the trends observed in the neutron imaging data using the insights gained with this thermal model. Revisiting Fig. 7, the heat produced by the cells is 1480 mW/cm² for 40°C, 1340 mW/cm² for 60°C, and 1290 mW/cm² for 80°C. In each case, heat production is sufficient to drive additional evaporation at a level consistent with a 15°C temperature rise. Assuming that a temperature rise of several degrees does occur in each case, the net rate of water production at constant current will decrease with increasing temperature, resulting in lower water content. This is the trend observed in Fig. 7; the results given in Fig. 8 show similar behavior, although the current density in the 40 and 80°C cases are slightly different.

In Fig. 9, the water content of a cell operating at 40°C is observed to continually increase with current. In Fig. 10, at 60°C, a maximum in water content is reached at an intermediate current density. These experimental results can be directly compared to the analytical results presented in Fig. 12. When local heating is present, the water content of a cell will depend on the competing processes of electrochemical water production and evaporative water removal.

Conclusions

The formation and distribution of water within an operating PEMFC was examined under transient conditions using neutron imaging. It was found that the water content of the cell responded much more slowly than the current density under dynamic conditions due to the characteristic time for liquid water transport being much greater than that for current conduction. The cell water content reaches steady state within 100–200 s following an instantaneous step increase in current from 0 to 1000 mA/cm². When the current load was ceased, the water content of the cell decreased slowly and in the course of a 600 s experiment, was not observed to reach a steady value.

The distribution of liquid water within the cell was found to be at a minimum near the cell inlet. Water content reaches a maximum in the center of the cell and decreases toward the gas flow exit. This nonuniform distribution was found to be time-dependent insofar as the cell requires a certain amount of time to reach steady state following a change in load.

Liquid water content and its distribution were found to be strongly affected by cell temperature and local heating. The water content of a cell operating at 1250 mA/cm² decreased as the cell temperature was increased from 40 to 60°C, and then further to 80°C. This effect was attributed to local heating within the cell, which influences the capacity of the cathode gas flow to carry water vapor. As cell temperature increases, additional liquid water can evaporate and be removed from the cell in the vapor phase, leading to a decrease in liquid water content. The change in cell water content as a function of current density was observed for cells operating at 40 and 60°C. In the case of the 40°C cell, the water content rose with cell current from OCV to 1250 mA/cm². The 60°C case showed an initial rise in water content with current reaching a maximum at 650 mA/cm². The cell water content then declined with a further increase in current density between 650 and 1250 mA/cm². This is attributed to the effects associated with local heating and the formation of water by the cell reaction, which are competing processes the relative magnitude of which change with temperature.

Acknowledgments

Sandia is a multiprogram laboratory operated by Sandia Corporation, a Lockheed Martin Company, for the United States Department of Energy's National Nuclear Security Administration under contract DE-AC04-94AL85000. This work was supported by Sandia National Laboratories Laboratory Directed Research and Development (LDRD) program, the U.S. Department of Commerce, the NIST Ionizing Radiation Division, the Director's office of NIST, the NIST Center for Neutron Research, and the Department of Energy through interagency agreement no. DE-AI01-01EE50660.

Sandia National Laboratories assisted in meeting the publication costs of this article.

List of Symbols

| | |
|---|---|
| F | Faraday's constant, 96,485 C/mol e ⁻ |
| h_{evap} | heat of vaporization of water, J/g |
| J | current, A |
| j | current density, A/cm ² |
| $\dot{m}_{\text{H}_2\text{O}}$ | mass flow rate of water vapor, g/s |
| \dot{m}_{air} | mass flow rate of air, g/s |
| $\dot{m}_{\text{H}_2\text{O}}^{\text{net}}$ | net cathode water production rate, g/s |
| $M_{\text{H}_2\text{O}}$ | molecular weight of water, 18 g/mol |
| M_{air} | molecular weight of air, 28.97 g/mol |
| P_v | vapor pressure, Pa |
| P_{tot} | total absolute pressure, Pa |
| \dot{Q}_{evap} | heat rate required for sensible heating and evaporation, J/s |
| \dot{Q}_{cell} | rate of heat production by the fuel cell, J/s |
| T | temperature, K |
| V_{cell} | cell operating voltage, V |
| V_{HHV} | energy content of hydrogen based on the higher heating value, V |
| $\Delta V_{\text{H}_2\text{O}}$ | change in water volume, mL |
| ω | humidity ratio, g-H ₂ O/g-air |

References

1. K. Tüber, D. Pócza, and C. Hebling, *J. Power Sources*, **124**, 403 (2003).
2. X. G. Yang, F. Y. Zhang, A. L. Lubawy, and C. Y. Wang, *Electrochem. Solid-State Lett.*, **7**, A408 (2004).
3. K. W. Feindel, L.P.-A. LaRocque, D. Starke, S. H. Bergens, and R. E. Wasylshen, *J. Am. Chem. Soc.*, **126**, 11436 (2004).
4. R. J. Bellows, M. Y. Lin, M. Arif, A. K. Thompson, and D. Jacobson, *J. Electrochem. Soc.*, **146**, 1099 (1999).
5. A. B. Geiger, A. Tsukada, E. Lehmann, P. Vontobel, A. Wokaun, and G. G. Scherer, *Fuel Cells*, **2**, 92 (2002).
6. D. Kramer, E. Lehmann, G. Frei, P. Vontobel, A. Wokaun, and G. G. Scherer, *Nucl. Instrum. Methods Phys. Res. A*, **542**, 52 (2005).
7. D. Kramer, J. Zhang, R. Shimoi, E. Lehmann, A. Wokaun, K. Shinohara, and G. G. Scherer, *Electrochim. Acta*, **50**, 2603 (2005).
8. N. Pekula, K. Heller, P. A. Chuang, A. Turhan, M. M. Mench, J. S. Brenizer, and K. Ünlü, *Nucl. Instrum. Methods Phys. Res. A*, **542**, 134 (2005).
9. P. A. Chuang, A. Turhan, A. K. Heller, J. S. Brenizer, T. A. Trabold, and M. M. Mench, in *FUEL CELL 2005, 3rd International Conference on Fuel Cell Science, Engineering and Technology*, pp. 31–37, ASME Proceedings, New York (2005).
10. R. Satija, D. L. Jacobson, M. Arif, and S. A. Werner, *J. Power Sources*, **129**, 238 (2004).
11. M. S. Wilson, J. A. Valerio, and S. Gottesfeld, *Electrochim. Acta*, **40**, 355 (1995).
12. S. Mazumder and J. V. Cole, *J. Electrochem. Soc.*, **150**, A1510 (2003).
13. M. M. Mench, C. Y. Wang, and M. Ishikawa, *J. Electrochem. Soc.*, **150**, A1052 (2003).
14. J. Larminie and A. Dicks, *Fuel Cells Explained*, 2nd ed., John Wiley & Sons, Ltd., West Sussex, England (2003).
15. M. M. Mench, D. J. Buford, and T. W. Davis, in *IMECE, 3rd International Mechanical Engineering Congress & Exposition*, Vol. 374, pp. 415–428, ASME Proceedings, New York (2003).
16. E. Birgersson, M. Noponen, and M. Vynnychy, *J. Electrochem. Soc.*, **152**, A1021 (2005).